This is a repository copy of *First Measurement of $\Lambda$ Electroproduction off Nuclei in the Current and Target Fragmentation Regions*.

White Rose Research Online URL for this paper:
https://eprints.whiterose.ac.uk/200243/

**Preprint:**
(2022) First Measurement of $\Lambda$ Electroproduction off Nuclei in the Current and Target Fragmentation Regions. [Preprint]

# First Measurement of Λ Electroproduction off Nuclei in the Current and Target Fragmentation Regions

T. Chetry,[29, 13] L. El Fassi,[29, *] W. K. Brooks,[44, 45, 46, 43] R. Dupré,[23] A. El Alaoui,[44] K. Hafidi,[1]

P. Achenbach,[43] K.P. Adhikari,[29] Z. Akbar,[52] W.R. Armstrong,[1] M. Arratia,[48] H. Atac,[42] H. Avakian,[43]

L. Baashen,[13] N.A. Baltzell,[43] L. Barion,[17] M. Bashkanov,[50] M. Battaglieri,[19] I. Bedlinskiy,[30] B. Benkel,[44]

F. Benmokhtar,[10] A. Bianconi,[47, 22] A.S. Biselli,[11, 4] M. Bondi,[20] W.A. Booth,[50] F. Bossù,[6] S. Boiarinov,[43]

K.-Th. Brinkmann,[36] W.J. Briscoe,[15] D. Bulumulla,[35] V.D. Burkert,[43] D.S. Carman,[43] J.C. Carvajal,[13]

A. Celentano,[19] P. Chatagnon,[43, 23] V. Chesnokov,[40, 34] G. Ciullo,[17, 12] P.L. Cole,[27, 5, 43] M. Contalbrigo,[17]

G. Costantini,[47, 22] A. D'Angelo,[20, 39] N. Dashyan,[54] R. De Vita,[19] M. Defurne,[6] A. Deur,[43] S. Diehl,[36, 8]

C. Djalali,[34, 41] H. Egiyan,[43] L. Elouadrhiri,[43] P. Eugenio,[14] S. Fegan,[50] A. Filippi,[21] G. Gavalian,[43, 31]

Y. Ghandilyan,[54] G.P. Gilfoyle,[38] D.I. Glazier,[49] A.A. Golubenko,[40] G. Gosta,[47] R.W. Gothe,[41] K.A. Griffioen,[53]

M. Guidal,[23] L. Guo,[13] H. Hakobyan,[44] M. Hattawy,[35] T.B. Hayward,[8] D. Heddle,[7, 43] A. Hobart,[23] M. Holtrop,[31]

Y. Ilieva,[41] D.G. Ireland,[49] E.L. Isupov,[40] D. Jenkins,[51] H.S. Jo,[26] M. L. Kabir,[29] A. Khanal,[13] M. Khandaker,[33, †]

A. Kim,[8] W. Kim,[26] F.J. Klein,[5] A. Kripko,[36] V. Kubarovsky,[43, 37] V. Lagerquist,[35] L. Lanza,[20] M. Leali,[47, 22]

S. Lee,[1] P. Lenisa,[17, 12] X. Li,[28] K. Livingston,[49] I .J .D. MacGregor,[49] D. Marchand,[23] V. Mascagna,[47, 22]

B. McKinnon,[49] C. McLauchlin,[41] Z.E. Meziani,[1, 42] S. Migliorati,[47, 22] T. Mineeva,[44] M. Mirazita,[18] V. Mokeev,[43]

C. Munoz Camacho,[23] P. Nadel-Turonski,[43] K. Neupane,[41] S. Niccolai,[23] M. Nicol,[50] G. Niculescu,[25]

M. Osipenko,[19] A.I. Ostrovidov,[14] P. Pandey,[35] M. Paolone,[32] L.L. Pappalardo,[17, 12] R. Paremuzyan,[43, 31]

E. Pasyuk,[43] S.J. Paul,[48] W. Phelps,[7, 15] N. Pilleux,[23] M. Pokhrel,[35] J. Poudel,[35] J.W. Price,[2] Y. Prok,[35, 52]

B.A. Raue,[13] T. Reed,[13] J. Richards,[8] M. Ripani,[19] J. Ritman,[16, 24] G. Rosner,[49] F. Sabatié,[6] C. Salgado,[33]

S. Schadmand,[16] A. Schmidt,[15, 28] R.A. Schumacher,[4] Y.G. Sharabian,[43] E.V. Shirokov,[40] U. Shrestha,[8]

P. Simmerling,[8] D. Sokhan,[6, 49] N. Sparveris,[42] S. Stepanyan,[43] I.I. Strakovsky,[15] S. Strauch,[41, 15] J.A. Tan,[26]

N. Trotta,[8] R. Tyson,[49] M. Ungaro,[43, 37] S. Vallarino,[17] L. Venturelli,[47, 22] H. Voskanyan,[54] E. Voutier,[23] X. Wei,[43]

L.B. Weinstein,[35] R. Williams,[50] R. Wishart,[49] M.H. Wood,[3, 41] N. Zachariou,[50] Z.W. Zhao,[9, 35] and M. Zurek[1]

(The CLAS Collaboration)

[1]*Argonne National Laboratory, Argonne, Illinois 60439*
[2]*California State University, Dominguez Hills, Carson, CA 90747*
[3]*Canisius College, Buffalo, NY*
[4]*Carnegie Mellon University, Pittsburgh, Pennsylvania 15213*
[5]*Catholic University of America, Washington, D.C. 20064*
[6]*IRFU, CEA, Université Paris-Saclay, F-91191 Gif-sur-Yvette, France*
[7]*Christopher Newport University, Newport News, Virginia 23606*
[8]*University of Connecticut, Storrs, Connecticut 06269*
[9]*Duke University, Durham, North Carolina 27708-0305*
[10]*Duquesne University, 600 Forbes Avenue, Pittsburgh, PA 15282*
[11]*Fairfield University, Fairfield CT 06824*
[12]*Universita' di Ferrara , 44121 Ferrara, Italy*
[13]*Florida International University, Miami, Florida 33199*
[14]*Florida State University, Tallahassee, Florida 32306*
[15]*The George Washington University, Washington, DC 20052*
[16]*GSI Helmholtzzentrum fur Schwerionenforschung GmbH, D-64291 Darmstadt, Germany*
[17]*INFN, Sezione di Ferrara, 44100 Ferrara, Italy*
[18]*INFN, Laboratori Nazionali di Frascati, 00044 Frascati, Italy*
[19]*INFN, Sezione di Genova, 16146 Genova, Italy*
[20]*INFN, Sezione di Roma Tor Vergata, 00133 Rome, Italy*
[21]*INFN, Sezione di Torino, 10125 Torino, Italy*
[22]*INFN, Sezione di Pavia, 27100 Pavia, Italy*
[23]*Universit'e Paris-Saclay, CNRS/IN2P3, IJCLab, 91405 Orsay, France*
[24]*Institute fur Kernphysik (Juelich), Juelich, Germany*
[25]*James Madison University, Harrisonburg, Virginia 22807*
[26]*Kyungpook National University, Daegu 41566, Republic of Korea*
[27]*Lamar University, 4400 MLK Blvd, PO Box 10046, Beaumont, Texas 77710*
[28]*Massachusetts Institute of Technology, Cambridge, Massachusetts 02139-4307*
[29]*Mississippi State University, Mississippi State, MS 39762-5167*
[30]*National Research Centre Kurchatov Institute - ITEP, Moscow, 117259, Russia*
[31]*University of New Hampshire, Durham, New Hampshire 03824-3568*

$^{32}$ New Mexico State University, PO Box 30001, Las Cruces, NM 88003, USA
$^{33}$ Norfolk State University, Norfolk, Virginia 23504
$^{34}$ Ohio University, Athens, Ohio 45701
$^{35}$ Old Dominion University, Norfolk, Virginia 23529
$^{36}$ II Physikalisches Institut der Universitaet Giessen, 35392 Giessen, Germany
$^{37}$ Rensselaer Polytechnic Institute, Troy, New York 12180-3590
$^{38}$ University of Richmond, Richmond, Virginia 23173
$^{39}$ Universita' di Roma Tor Vergata, 00133 Rome Italy
$^{40}$ Skobeltsyn Institute of Nuclear Physics, Lomonosov Moscow State University, 119234 Moscow, Russia
$^{41}$ University of South Carolina, Columbia, South Carolina 29208
$^{42}$ Temple University, Philadelphia, PA 19122
$^{43}$ Thomas Jefferson National Accelerator Facility, Newport News, Virginia 23606
$^{44}$ Universidad Técnica Federico Santa María, Casilla 110-V Valparaíso, Chile
$^{45}$ Center for Science and Technology of Valparaíso, Valparaíso, Chile
$^{46}$ SAPHIR Millennium Science Institute, Santiago, Chile
$^{47}$ Universit'a degli Studi di Brescia, 25123 Brescia, Italy
$^{48}$ University of California Riverside, 900 University Avenue, Riverside, CA 92521, USA
$^{49}$ University of Glasgow, Glasgow G12 8QQ, United Kingdom
$^{50}$ University of York, York YO10 5DD, United Kingdom
$^{51}$ Virginia Tech, Blacksburg, Virginia 24061-0435
$^{52}$ University of Virginia, Charlottesville, Virginia 22901
$^{53}$ College of William and Mary, Williamsburg, Virginia 23187-8795
$^{54}$ Yerevan Physics Institute, 375036 Yerevan, Armenia
(Dated: October 26, 2022)

We report results of $\Lambda$ hyperon production in semi-inclusive deep-inelastic scattering off deuterium, carbon, iron, and lead targets obtained with the CLAS detector and the CEBAF 5.014 GeV electron beam. These results represent the first measurements of the $\Lambda$ multiplicity ratio and transverse momentum broadening as a function of the energy fraction ($z$) in the current and target fragmentation regions. The multiplicity ratio exhibits a strong suppression at high $z$ and an enhancement at low $z$. The measured transverse momentum broadening is an order of magnitude greater than that seen for light mesons. This indicates that the propagating entity interacts very strongly with the nuclear medium, which suggests that propagation of di-quark configurations in the nuclear medium takes place at least part of the time, even at high $z$. The trends of these results are qualitatively described by the GiBUU transport model, particularly for the multiplicity ratios. These observations will potentially open a new era of studies of the structure of the nucleon as well as of strange baryons.

The study of the underlying structure of hadrons suggests a dynamical origin of the strong interactions between the confined color objects, quarks and gluons (partons), the building blocks of nuclei. Given that the description of the non-perturbative transition from partonic degrees of freedom to ordinary hadrons cannot be performed within the perturbative Quantum Chromo-Dynamics (QCD) or lattice QCD frameworks, pure phenomenological methods are explored to study low-energy phenomena such as the hadronization process [1, 2]. To this end, deep inelastic electron-nucleon scattering (DIS) has been utilized as a pioneering process on atomic nuclei to access the modified parton distributions, test the hadronization mechanisms, and study color confinement dynamics in the cold nuclear medium [3–5]. In this regime, when the electron emits an energetic virtual-photon ($\gamma^*$) that removes the struck quark from the rest of the residual system, it takes a finite time until the reaction products hadronize. These products would, in lepton-nucleus scattering, interact with the surrounding nuclear medium during the formation time, which is approximated at intermediate energies to be of a similar order as nuclear radii [6]. The target nucleus acts then as a

femtoscope with unique analyzing power that allows for the extraction of the hadronization time-distance scales. Therefore, the study of scattering off nuclei with different sizes and at various $\gamma^*$ kinematics probes the space-time evolution of the hadronization mechanism related to the quark propagation and the color field restoration to form regular hadrons [7, 8].

As depicted in Fig. 1, the hadronization process is characterized by two time-scales describing its two phases. After the virtual photon hard scattering, during the production time ($\tau_p$), the struck quark propagates in the medium as a colored object and thus emits gluons (even in vacuum). This quark then transforms into a colorless object, referred to as a prehadron, which eventually evolves into a fully dressed hadron within the formation time ($\tau_f$). The hadronization studies are thus performed to provide information on the dynamics scales of the process, and to constrain the existing models that provide different predictions of its time characteristics either in vacuum or in nuclei [9–13]. In principle, the production and formation mechanisms are the same for both cases with the exception that in the former, the $q\bar{q}$ pairs or $qqq$ systems are considered emerging from the vacuum
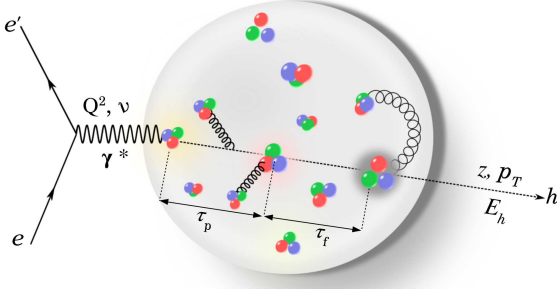
Figure 1. An illustration of the hadronization process as well as its production, $\tau_p$, and formation, $\tau_f$, time-scales. $\nu = E_e - E_{e'}$ is the $\gamma^*$ energy transferred to the struck quark, $Q^2$ is the four-momentum transfer squared, $z = E_h/\nu$ is the fractional energy of the observed hadron, $h$, where $E_h$ is the hadron's energy in the lab frame, and $p_T$ is the hadron's transverse momentum with respect to the virtual-photon direction (see Fig. 2 top-right).

before expanding into color singlet hadrons, while in the latter, the struck quark is propagating and can pick up its partner(s) from the medium. In this case, the presence of the medium will lead to several modifications and in-medium stimulated effects related either to the struck quark, formed prehadron, and/or hadron interactions with their surroundings.

The study of hadronization mechanisms is done in the framework of semi-inclusive DIS (SIDIS), and its characteristics are probed via the measurement of two experimental observables. The first is the hadron multiplicity ratio, $R_h^A$, which is defined as

$$R_h^A(\nu, Q^2, z, p_T^2) = \frac{N_h^A(\nu, Q^2, z, p_T^2)/N_e^A(\nu, Q^2)}{N_h^D(\nu, Q^2, z, p_T^2)/N_e^D(\nu, Q^2)}, \quad (1)$$

where $N_e^A$ and $N_h^A$ are, respectively, the scattered electron and SIDIS hadron yields produced on a target $A$ and corrected for detector acceptance and reconstruction efficiency. The variables $\nu$, $Q^2$, $z$, and $p_T$ are defined in Fig. 1. The multiplicity ratio is normalized by DIS electrons originating from corresponding targets to cancel, to some extent, the initial-state nuclear effects and thus correct for the European Muon Collaboration (EMC) effect [7]. $R_h^A$ quantifies to which extent hadrons are attenuated at a given kinematics as was reported in earlier studies by SLAC [3], HERMES [14–18], and EMC [4] due to the (pre)hadron elastic or inelastic scattering and/or the energy loss of the hadron-fragmented struck quark during the color-neutralization stage preceding hadron formation.

The second observable is the transverse momentum broadening, $\Delta p_T^2$, defined as

$$\Delta p_T^2 = \langle p_T^2 \rangle_A - \langle p_T^2 \rangle_D, \quad (2)$$

where $\langle p_T^2 \rangle_A$ is the mean $p_T$ squared for a target $A$ (see Fig. 2 bottom-right). This observable carries crucial in-

formation about the interaction of the propagating parton with the surrounding color field in the nucleus. Several models correlate the $p_T$-broadening with the parton energy loss triggered by the stimulated gluon bremsstrahlung while crossing the medium in the color-neutralization stage [19, 20]. Based on the perturbative view of the Lund string model, the propagating quark's energy loss is predicted to be at a rate comparable to its string constant on the order of 1 GeV/fm [9, 21]. This effect is believed to be the reason behind the observed jet quenching in heavy-ion collisions at the Relativistic Heavy Ion Collider and at the Large Hadron Collider, leading to the suppression of large $p_T$ hadron production in nucleus-nucleus compared to proton-proton collisions [22, 23].

In this Letter, results on SIDIS production of $\Lambda$ hyperons off nuclei, i.e., $e+A \rightarrow e'+\Lambda+X$, are reported, where $A$ is the heavy nuclear target or deuterium, $X$ is the unobserved hadronic system, and $\Lambda$ is identified in the final state through its decay products $\pi^-$ and $p$. The results represent the first-ever measurement of $\Lambda$ multiplicity ratios and $p_T$-broadening as a function of $z$ and the atomic mass-number, $A$, for the latter in the current (forward) fragmentation region, in which the struck (di-) quark initiates the hadronization process, and the target (backward) fragmentation region, in which the target remnant moves reciprocally with regard to the $\gamma^*$ direction undergoing a spectator or target fragmentation. Furthermore, the current and target fragmentation processes are assumed to have dominant contributions in distinct phase space regions, which are kinematically separated via the coverage of the Feynman scaling variable $x_F$ [24, 25].

Previous measurements of $R_h^A$ for various hadrons, mainly mesons and (anti-) protons by the HERMES [14–18] and the CLAS [26, 27] Collaborations have reported a strong suppression of leading hadrons at high $z$ and a slight enhancement of multiplicity ratios at low $z$ while scanning heavy to light nuclei. This inverted effect for slow (backward) and fast (forward) protons in HERMES results, the sole baryon study so far, demonstrates the importance of separating the two regions to properly interpret the data. Approximate separation is possible via the $z$-dependence of Feynman $x_F$ [28] given that the current fragmentation (high $z$) is dominated by positive $x_F$, while the target remnant favors negative $x_F$ [24, 25, 29].

A study of $\Delta p_T^2$ for mesons was also performed by the HERMES experiment [17], but its finding could not distinguish between models predicting an $A^{1/3}$ or $A^{2/3}$ mass-dependence [19, 20]. The $\Delta p_T^2$ is expected to increase linearly as $A^{1/3}$ if it is proportional to the nuclear radius and thus the crossed path length, $L$, in the nuclear medium. While, an increase as $A^{2/3}$ would indicate a dependence on partonic energy loss via the prediction that $\frac{\Delta E}{dx} \propto \Delta p_T^2$ and thus $\Delta E \propto L^2$ [19].

The data presented in this paper were collected during early 2004. An electron beam of 5.014 GeV energy was

incident simultaneously on a 2-cm-long liquid-deuterium target (LD2) and a 3 mm diameter solid target (carbon, iron, or lead). A remotely controlled dual-target system [30] was used to reduce systematic uncertainties and allow high-precision measurements of various experimental observables [27, 31]. The cryogenic and solid targets were located 4 cm apart to minimize the difference in CLAS acceptance, while maintaining the ability to identify event-by-event the target where the interaction occurred via vertex reconstruction [32]. The thickness of each solid target (1.72 mm for C, 0.4 mm for Fe, and 0.14 mm for Pb) was chosen so that all targets including deuterium would have comparable per-nucleon luminosities ($\sim 10^{34}$ cm$^{-2}$s$^{-1}$). The scattered electrons, negative pions, and protons were detected in coincidence using the CLAS spectrometer [33]. The scattered electrons were identified requiring a coincidence between the Cherenkov counter and the electromagnetic calorimeter signals [31], while pions and protons were identified through time-of-flight measurements [31, 32, 34].

The $\Lambda$ hyperons were identified through the reconstructed invariant mass of detected pions and protons (see SP.1 for more details about $\Lambda$ identification method [35]). For each event, several kinematic variables were evaluated including $Q^2$, the virtual photon-nucleon invariant mass squared $W^2$, and the $\gamma^*$ energy fraction $y = \nu/E_e$, where $E_e$ is the incident beam energy. The

SIDIS $\Lambda$ events were selected with $Q^2 > 1$ GeV$^2$ to probe the nucleon structure, $W > 2$ GeV to suppress contamination from the resonance region, and $y < 0.85$ to reduce the size of radiative effects on the extracted multiplicity ratios based on the HERMES studies [14–18]. The $(p, \pi^-)$ invariant mass distributions are shown in Fig. 2 left for iron (top) and LD2 (bottom) with all cuts applied. The distributions exhibit a clean $\Lambda$ peak positioned around 1115.7 MeV sitting on a substantial combinatorial background (CB). An advanced data modeling and fitting toolkit RooFit [36] was used along with the event mixing technique to subtract the CB (red dotted curves in Fig. 2 left), which is reconstructed by combining uncorrelated $p$ and $\pi^-$ tracks from different events [37]. The extraction of the background-subtracted $\Lambda$ yields, as well as the $p_T^2$ means, was performed after weighting their distributions event-by-event with the inverse of the acceptance correction (AC) factors. The latter were evaluated using events generated with the Pythia event generator [38] and processed by the CLAS GEANT3 package [39] to simulate the detector geometrical acceptance, as well as the associated detection and reconstruction efficiencies. Pythia was modified to include nuclear parton distribution functions [40] and Fermi motion based on the Paris potential distribution and realistic many-body calculations [41]. Radiative effects were also included in the simulation using the RadGen code [42] developed to correct lepton-nucleon scattering observables from Quantum Electrodynamics radiative processes. Small corrections were also applied for other effects related to proton energy loss, scattering angle and momentum distortions, vertex misalignment [32, 34], and LD2 endcap contamination.

Due to the limited statistics of the $\Lambda$ production channel, the extractions of both multiplicity ratios and $p_T$-broadening results were performed by integrating over all kinematic variables except $z$, which is divided into the six bins shown in Table S2 [35]. Given that the interest in this work is in the $z$ and $A$ dependencies of the observables, the systematic uncertainties were separated into point-to-point (p2p), which exhibit some $z$ and $A$ dependencies, and normalization uncertainties, which are kinematics independent. An in-depth study was carried out and the main systematic sources are related to 1) particle identification cuts to identify the three final-state particles, scattered electron, $p$, and $\pi^-$, 2) dual-target vertex corrections, 3) AC multidimensional (6D) map variables and the binning that was chosen based on the comparison of experimental data and simulation, 4) AC weight cuts to suppress artificial spikes due to poor statistics in some AC 6D bins, 5) CB subtraction methods by varying the event mixing uncorrelated track combinations and BW shapes utilized in RooFit for $R_\Lambda^A$ while considering CB sideband subtraction for $\Delta p_T^2$, 6) $\Lambda$ mass range for $R_\Lambda^A$, and 7) LD2 endcaps and radiative correction procedures. As a result, the total p2p (normalization) un-
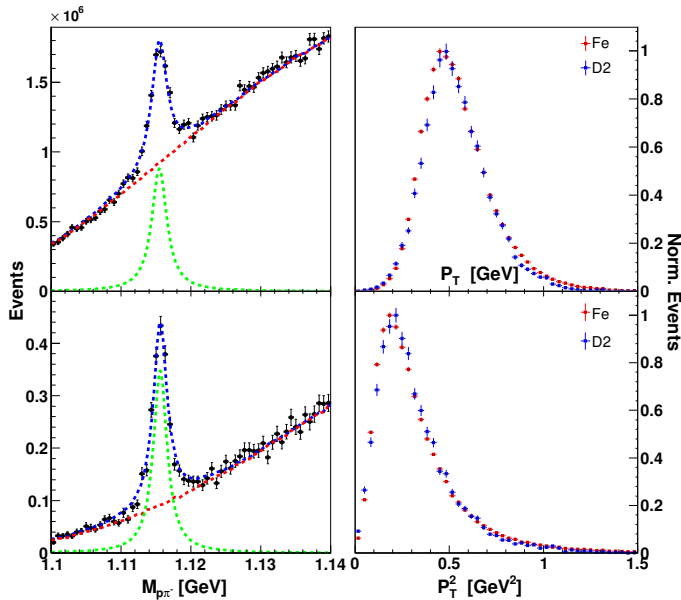


Figure 2. Left: Acceptance-weighted $(p, \pi^-)$ invariant mass distributions for the Fe/LD2 (top/bottom) targets. Blue curves represent the RooFit $\chi^2$ minimization using a simple Breit-Wigner (BW) function for the $\Lambda$ signal and event mixing for the combinatorial background (red dotted curves). The green distributions are the fit results that are integrated to obtain the $\Lambda$ yields. Right: Comparison of Fe (red) and LD2 (blue) acceptance-weighted $p_T/p_T^2$ (top/bottom) normalized distributions to their peak height.

Figure 3. $\Lambda$ $z$-binned multiplicity ratios for carbon, iron, and lead (the results are horizontally shifted for clarity). The outer error bars are the p2p systematic uncertainties added in quadrature with the statistical uncertainties. The inset contains the total normalization uncertainties for each nucleus. The plots illustrate the results of the low (left) and high (right) $z$ ranges corresponding, respectively, to the target and current fragmentation regions. The curves correspond to GiBUU model calculations [43].

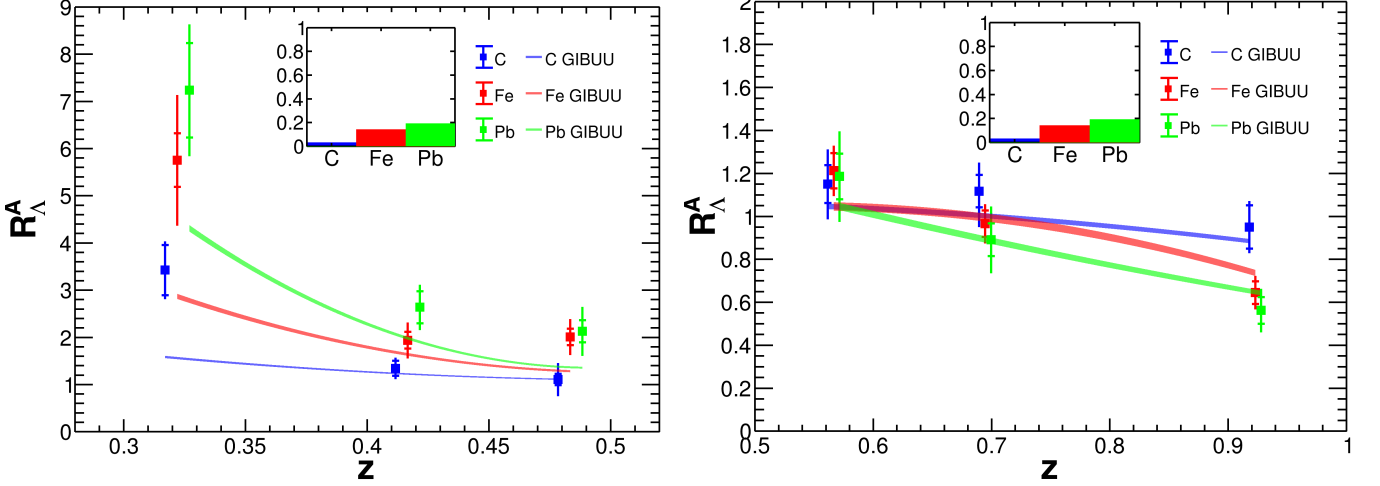certainties vary between 6% to 30% (less than 3%) for the multiplicity ratios of all nuclei with the dominant contributions from the AC and CB subtraction methods (see Table S3 [35]). Similarly, the total p2p uncertainties vary between 10% (1.4%) and 81% (8.5%) for the nuclear $z$ ($A$) dependence of $p_T$-broadening (see Table S4 (S5) [35]), while the total normalization uncertainty for both dependencies is less than 1%. The largest p2p $z$-dependent uncertainty, which is associated with the lead target, is still less than the 50% statistical uncertainty as shown in Fig. 3.

The $\Lambda$ multiplicity ratio results are depicted in Fig. 3 along with theoretical calculations from the GiBUU model [43]. As expected, $R_\Lambda^A$ manifests an inverted behavior in the two $z$-regions; at high $z$ (see Fig. 3 right), the region in which the current fragmentation dominates, $\Lambda$ baryons exhibit less attenuation in lighter nuclei and greater suppression with $z$, up to 40% in lead and 35% in iron at the highest $z$-bin. However, at low $z$ (see Fig. 3 left) $R_\Lambda^A$ is more enhanced on heavy nuclei as a signature of the significant contribution from the target fragmentation that predominates in this kinematic region. This observation is consistent with the fact that the $\Lambda$ baryons show a significant leading particle effect, $i.e.$, they carry a substantial fraction of the incoming proton momentum [44] and thus large negative $x_F$ (see Fig. S1 [35]) and small $p_T$ relative to the $\gamma^*$ direction [24, 25]. The data are qualitatively described by GiBUU for most of the $z$-range and most of the targets except for the lowest $z$-bin, where approximately a factor of two difference is observed.

Figure 4 contains the $\Lambda$ $p_T$-broadening results as a function of $z$ (left) and $A$ (right) along with theo-

retical calculations from the GiBUU model [43]. The monotonic increase of broadening with $z$ and the mass-number reflects the interaction of the propagating object with the surrounding color field in the nucleus during the neutralization stage and/or the elastic scattering of the prehadron and the fully formed $\Lambda$ [19, 20]. Such a (pre)hadron interaction, as well as broadening, seems to diminish at the highest $z$-bin. This is an indication of the partonic stage dominance of the hadronization process preceding the (pre)hadron formation, as their elastic scattering in the medium should have led to more broadening as $z$ approaches unity [17, 45]. This trend is in-favor of the $A^{1/3}$ dependence of $\Delta p_T^2$ and implies that the production time is within the nuclear medium. Yet, the measured $\Lambda$ hyperon broadening is an order of magnitude greater than that seen in the HERMES meson results [17]. This could be due to the quark-diquark nucleon structure so that the virtual photon, instead of being absorbed by a quark, is absorbed by a di-quark. That is to say, the propagating colored di-quark has a sizable mass and an extended QCD color field compared to a single quark, leading to more in-medium interactions, and thus an increase of the $\Delta p_T^2$ magnitude [46]. This di-quark scattering speculation offers a good explanation of the $R_\Lambda^A$ attenuation with increasing $z$ in the current fragmentation region. While GiBUU has reasonably described HERMES, EMC [6, 47, 48], and CLAS [26, 27] multiplicity ratio measurements, it underestimates our $\Lambda$ $p_T$-broadening results, which could indicate that the angular distribution is inaccurate in the initial elementary production process of $\Lambda$ or that the final state interactions in the current model's string fragmentation functions are not realistic [49].
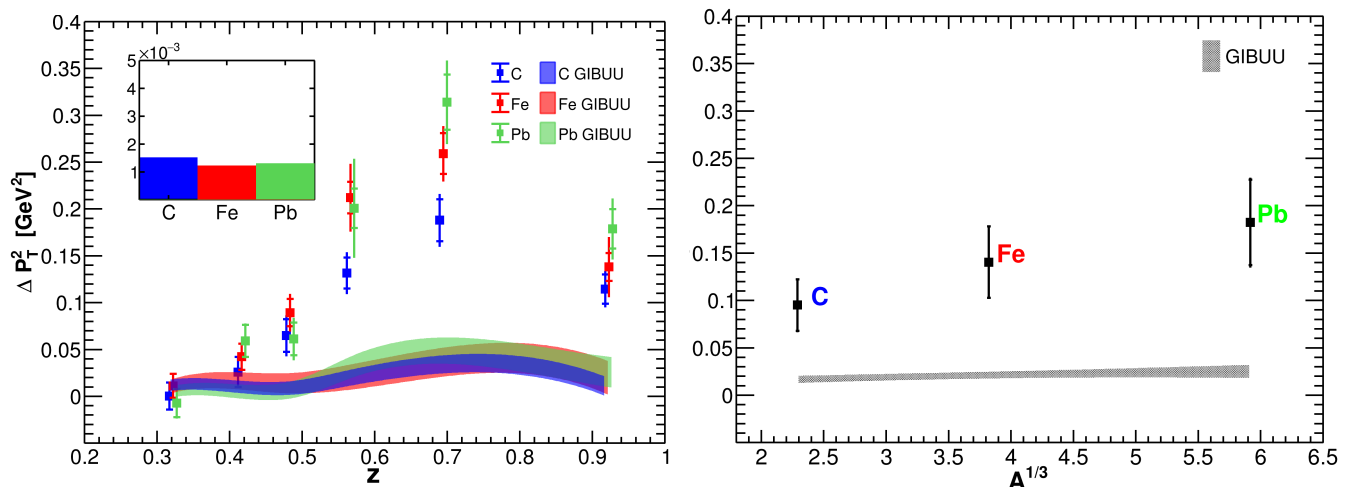
Figure 4. Left (right): The $z$ (nuclear radius)-dependent $\Delta p_T^2$ results for the three nuclei (results are horizontally shifted for clarity). The outer error bars are the p2p systematic uncertainties added in quadrature with the statistical uncertainties, while the normalization uncertainties are presented in the inset for the $z$-dependence and found to be less than 1% for the $A$-dependence. The GiBUU model calculations are represented by the colored (left) and shaded (right) bands obtained by interpolating the model points and their statistical uncertainties.

In summary, the first-ever measurement of $\Lambda$ multiplicity ratios and $p_T$-broadening as a function of $z$ and $A$ in the current and target fragmentation regions are reported. Both observables depend strongly on $z$, with an enhancement of $R_\Lambda^A$ at low $z$ and a suppression at high $z$ up to $0.951 \pm 0.125$ for carbon, $0.645 \pm 0.164$ for iron, and $0.562 \pm 0.219$ for lead, and an increase of $p_T$-broadening with $A$ and $z$ except for the last $z$-bin where the broadening starts decreasing due to the partonic stage dominance of the hadronization process. The one order of magnitude larger broadening for this hyperon channel compared to HERMES meson results, as well as the strong suppression of $R_\Lambda^A$ at high $z$, suggests the possibility of a direct scattering off di-quark configurations of the nucleon. The multiplicity ratio results are qualitatively described by the GiBUU transport model, however, the model strongly underestimates our $p_T$-broadening results. This finding has the potential to stimulate further experimental and theoretical investigations, constrain existing models such as GiBUU, and open a new era of studies of the nucleon and light hyperon structure.

Future higher-luminosity measurements with CLAS12 and an 11 GeV beam energy [50] will study SIDIS production of a variety of mesons and baryons over a wide kinematic range. This is crucial to constrain competing models and boost our understanding of the fragmentation mechanisms that lead to the formation of various hadrons. It would also provide an opportunity to study for the $\Lambda$ SIDIS final states the correlation between kaons and $\Lambda$s that will presumably be sensitive to the di-quark structure in the struck nucleon. The forthcoming experiments with CLAS12, in addition to measurements at the planned Electron Ion Collider [51], have the potential to investigate in great detail the speculated di-quark scattering in the current results, which would have a significant impact on our understanding of nucleon and baryon structure.

* le334@msstate.edu
† Current address: Idaho State University, Pocatello, Idaho 83209

[1] D. J. Gross and F. Wilczek, Ultraviolet behavior of non-abelian gauge theories, Phys. Rev. Lett. **30**, 1343 (1973).

[2] Y. L. Dokshitzer, QCD phenomenology (2003) pp. 1–33, arXiv:hep-ph/0306287.

[3] L. S. Osborne, C. Bolon, R. L. Lanza, D. Luckey, D. G. Roth, J. F. Martin, G. J. Feldman, M. E. B. Franklin, G. Hanson, and M. L. Perl, Electroproduction of Hadrons From Nuclei, Phys. Rev. Lett. **40**, 1624 (1978).

[4] J. Ashman et al. (European Muon Collaboration), Comparison of forward hadrons produced in muon interactions on nuclear targets and deuterium, Z. Phys. C **52**, 1 (1991).

[5] A. Arvidson et al. (European Muon Collaboration), Hadron production in 200-GeV $\mu$ - copper and $\mu$ - carbon deep inelastic interactions, Nucl. Phys. B **246**, 381 (1984).

[6] K. Gallmeister and U. Mosel, Time Dependent Hadronization via HERMES and EMC Data Consistency, Nucl. Phys. A **801**, 68 (2008).

[7] A. Accardi, F. Arleo, W. K. Brooks, D. D'Enterria, and V. Muccifora, Parton Propagation and Fragmentation in QCD Matter, Riv. Nuovo Cim. **32**, 439 (2009).

[8] W. K. Brooks and J. A. López, Estimating the color lifetime of energetic quarks, Phys. Lett. B **816**, 136171 (2021).

[9] B. Andersson, G. Gustafson, and C. Peterson, QUARK JET FRAGMENTATION, Phys. Scripta **19**, 184 (1979).

[10] X. Artru and G. Mennessier, String model and multiproduction, Nucl. Phys. B **70**, 93 (1974).

[11] E. V. Shuryak, Quark-Gluon Plasma and Hadronic Production of Leptons, Photons and Psions, Phys. Lett. B **78**, 150 (1978).

[12] X.-N. Wang, Why the observed jet quenching at RHIC is due to parton energy loss, Phys. Lett. B **579**, 299 (2004).

[13] B. Z. Kopeliovich, J. Nemchik, E. Predazzi, and A. Hayashigaki, Nuclear hadronization: Within or without?, Nucl. Phys. A **740**, 211 (2004).

[14] A. Airapetian et al. (HERMES Collaboration), Hadron formation in deep inelastic positron scattering in a nuclear environment, Eur. Phys. J. C **20**, 479 (2001).

[15] A. Airapetian et al. (HERMES Collaboration), Quark fragmentation to $\pi^{\pm}$, $\pi^0$, $K^{\pm}$, $p$ and $\bar{p}$ in the nuclear environment, Phys. Lett. B **577**, 37 (2003).

[16] A. Airapetian et al. (HERMES Collaboration), Hadronization in semi-inclusive deep-inelastic scattering on nuclei, Nucl. Phys. B **780**, 1 (2007).

[17] A. Airapetian et al. (HERMES Collaboration), Transverse momentum broadening of hadrons produced in semi-inclusive deep-inelastic scattering on nuclei, Phys. Lett. B **684**, 114 (2010).

[18] A. Airapetian et al. (HERMES Collaboration), Multidimensional Study of Hadronization in Nuclei, Eur. Phys. J. A **47**, 113 (2011).

[19] R. Baier, Y. L. Dokshitzer, A. H. Mueller, S. Peigne, and D. Schiff, Radiative energy loss and p(T) broadening of high-energy partons in nuclei, Nucl. Phys. B **484**, 265 (1997).

[20] S. J. Brodsky and P. Hoyer, A Bound on the energy loss of partons in nuclei, Phys. Lett. B **298**, 165 (1993).

[21] B. Andersson, G. Gustafson, G. Ingelman, and T. Sjostrand, Parton Fragmentation and String Dynamics, Phys. Rept. **97**, 31 (1983).

[22] J. Adams et al. (STAR Collaboration), Incident energy dependence of pt correlations at RHIC, Phys. Rev. C **72**, 044902 (2005).

[23] K. Adcox et al. (PHENIX Collaboration), Formation of dense partonic matter in relativistic nucleus-nucleus collisions at RHIC: Experimental evaluation by the PHENIX collaboration, Nucl. Phys. A **757**, 184 (2005).

[24] F. A. Ceccopieri and D. Mancusi, QCD analysis of Lambda hyperon production in DIS target-fragmentation region, Eur. Phys. J. C **73**, 2435 (2013).

[25] F. A. Ceccopieri, Lambda production in the DIS target fragmentation region, Eur. Phys. J. C **76**, 69 (2016).

[26] A. Daniel et al. (CLAS Collaboration), Measurement of the nuclear multiplicity ratio for $K_s^0$ hadronization at CLAS, Phys. Lett. B **706**, 26 (2011).

[27] S. Morán et al. (CLAS Collaboration), Measurement of charged-pion production in deep-inelastic scattering off nuclei with the clas detector, Phys. Rev. C **105**, 015201 (2022).

[28] The frame-dependent Feynman variable $x_F = p_L^*/p_L^{*max}$ is defined as the fraction of the center-of-mass longitudinal momentum carried by the hadron with respect to the $\gamma^*$ direction in the lab frame.

[29] D. Graudenz, One particle inclusive processes in deeply inelastic lepton - nucleon scattering, Nucl. Phys. B **432**, 351 (1994).

[30] H. Hakobyan et al., A double-target system for precision measurements of nuclear medium effects, Nucl. Instrum. Meth. A **592**, 218 (2008).

[31] L. El Fassi et al. (CLAS Collaboration), Evidence for the onset of color transparency in $\rho^0$ electroproduction off nuclei, Phys. Lett. B **712**, 326 (2012).

[32] B. Schmookler et al. (CLAS Collaboration), Modified structure of protons and neutrons in correlated pairs, Nature **566**, 354 (2019).

[33] B. A. Mecking et al., The CEBAF large acceptance spectrometer (CLAS), Nucl. Instrum. Meth. **503**, 513 (2003).

[34] O. Hen et al. (CLAS Collaboration), Measurement of transparency ratios for protons from short-range correlated pairs, Phys. Lett. B **722**, 63 (2013).

[35] See SUPPLEMENTARY MATERIAL.

[36] W. Verkerke and D. Kirkby, The roofit toolkit for data modeling (2003).

[37] T. Mineeva, Hadronization Studies via $\pi^0$ Electroproduction off D, C, Fe, and Pb (2013).

[38] K. Gallmeister and T. Falter, Space-time picture of fragmentation in PYTHIA/JETSET for HERMES and RHIC, Phys. Lett. B **630**, 40 (2005).

[39] E. Wolin, GSIM User's Guide Version 1.1 (1996).

[40] A. Buckley, J. Ferrando, S. Lloyd, K. Nordström, B. Page, M. Rüfenacht, M. Schönherr, and G. Watt, LHAPDF6: parton density access in the LHC precision era, Eur. Phys. J. C **75**, 132 (2015).

[41] C. Ciofi degli Atti and S. Simula, Realistic model of the nucleon spectral function in few and many nucleon systems, Phys. Rev. C **53**, 1689 (1996).

[42] I. Akushevich, H. Bottcher, and D. Ryckbosch, RAD-GEN 1.0: Monte Carlo generator for radiative events in DIS on polarized and unpolarized targets, in *Work-*

shop on Monte Carlo Generators for HERA Physics (Plenary Starting Meeting) (1998) pp. 554–565, arXiv:hep-ph/9906408.

[43] O. Buss, T. Gaitanos, K. Gallmeister, H. van Hees, M. Kaskulov, O. Lalakulich, A. B. Larionov, T. Leitner, J. Weil, and U. Mosel, Transport-theoretical Description of Nuclear Reactions, Phys. Rept. **512**, 1 (2012).

[44] By convention of the $\gamma^* p$ frame, a negative longitudinal momentum fraction $x_F$ corresponds to final state hadrons moving parallel to the incoming proton direction, thus covering the low $z$ region. However, the positive $x_F$ favors high $z$, where forward fragmentation governs.

[45] P. Di Nezza, Nuclear attenuation and p(t) broadening in DIS at HERMES, J. Phys. Conf. Ser. **110**, 032009 (2008).

[46] M. Barabanov, M. Bedolla, W. Brooks, G. Cates, C. Chen, Y. Chen, E. Cisbani, M. Ding, G. Eichmann, R. Ent, J. Ferretti, R. Gothe, T. Horn, S. Liuti, C. Mezrag, A. Pilloni, A. Puckett, C. Roberts, P. Rossi, and B. Wojtsekhowski, Diquark correlations in hadron physics: Origin, impact and evidence, Progress in Particle and Nuclear Physics **116**, 103835 (2021).

[47] T. Falter, W. Cassing, K. Gallmeister, and U. Mosel, Hadron formation and attenuation in deep inelastic lepton scattering off nuclei, Phys. Lett. B **594**, 61 (2004).

[48] T. Falter, W. Cassing, K. Gallmeister, and U. Mosel, Hadron attenuation in deep inelastic lepton-nucleus scattering, Phys. Rev. C **70**, 054609 (2004).

[49] K. Gallmeister and U. Mosel, private communication (2022).

[50] W. K. Brooks *et al.* (CLAS Collaboration), Quark propagation and hadron formation, E12-06-117 Experiment (2010).

[51] A. Accardi *et al.*, Electron-Ion Collider: The Next QCD Frontier, Eur. Phys. J. A **52**, 268 (2016).

# SUPPLEMENTARY MATERIAL

This appendix contains supplementary information about the $\Lambda$ identification method in SP.1, the acceptance correction details related to the multidimensional (6D) map variables and binning, weight definition and cut, and its application procedure in SP.2, a summary of the contributions of systematic effects to the total point-to-point uncertainty budget in SP.3, and the reported results in the last two figures of this manuscript as well as a supporting figure, Fig. S1, in SP.4. In Table S6, the $z$-binned multiplicity ratios are given for all nuclei, while Table S7 (Table S8) contains the transverse momentum broadening as a function of $z$ ($A$) for all nuclei.

**SP.1 Lambda Identification** In the sample of reconstructed SIDIS events originating from either the liquid or solid target, one scattered $e^-$ and at least one $\pi^-$ and $p$, the decay products of the $\Lambda$, were required. To reconstruct the $z$-binned ($\pi^-$, $p$) invariant mass spectrum for each target, the 4-vector energy-momentum ($P^\mu = (E, p_x, p_y, p_z)$) of all identified negatively charged pions and protons were combined event-by-event as

$$P_\Lambda = P_p + P_{\pi^-}, \tag{S1}$$

where $P_\Lambda$, $P_p$, and $P_{\pi^-}$ are the 4-vector energy-momentum of the $\Lambda$ candidates, protons, and $\pi^-$s, respectively. Figure 2 left shows the acceptance-weighted invariant mass from solid (top) and liquid (bottom) targets in which the $\Lambda$ peak sits on a huge combinatorial background (red dotted curves) that is subtracted using `RooFit` to extract the pure $\Lambda$ yields and thus obtain the presented multiplicity ratios in Fig. 3.

**SP.2 Acceptance Correction** The adopted acceptance correction for this analysis is based on a bin-by-bin correction method. Its main advantage is that it should be, in principle, independent of the model used in the Monte-Carlo (MC) event generator if the chosen bins are infinitely small. This is very important for this channel since it is not expected that the employed model in Pythia would be realistic enough to perfectly reproduce the data. Based on a comparison between MC and experimental data, the chosen AC six dimensional (6D) map variables and binning are summarized in Tables S1- S2.

| Variables | Range | Number of bins | Bin width |
|-----------|-------|----------------|-----------|
| $W$ [GeV] | 2.00 - 2.80 | 2 | 0.4 |
| $\nu$ | 2.25 - 4.25 | 3 | $0.\overline{6}$ |
| $\phi_{\pi^-}$ [deg] | 0.0 - 360.0 | 2 | 180 |
| $\phi_{e\Lambda}$ [deg] | 0.0 - 360.0 | 3 | 120 |
| $P_\Lambda$ [GeV] | 0.10 - 4.25 | 3 | $1.38\overline{3}$ |
| $z$ | 0.28 - 1.00 | 6 | see Table S2 |
| Total | | 648 | |

Table S1. Binning for the AC map, where $\nu$, $W$, and $z$ were already defined, $\phi_{\pi^-}$ is the $\pi^-$ azimuthal decay angle in the $\Lambda$ rest frame, $\phi_{e\Lambda}$ is the angle between the leptonic and hadronic planes, and $p_\Lambda$ is the $\Lambda$ momentum. Table S2 shows the $z$ bins used as reported in Table S6.

| $z-$bin $\#$ | 1 | 2 | 3 | 4 | 5 | 6 |
|--------------|---|---|---|---|---|---|
| $z_{min}$ | 0.28 | 0.38 | 0.44 | 0.51 | 0.60 | 0.75 |
| $z_{max}$ | 0.38 | 0.44 | 0.51 | 0.60 | 0.75 | 1.00 |

Table S2. The $z$ bins used in this analysis.

The acceptance correction factors are defined for each 6D bin $k= (W, \nu, p_\Lambda, \phi_{\pi^-}, \phi_{e\Lambda}, z)$ as

$$AC_k = \frac{N_{acc}(W, \nu, p_\Lambda, \phi_{\pi^-}, \phi_{e\Lambda}, z)}{N_{gen}(W, \nu, p_\Lambda, \phi_{\pi^-}, \phi_{e\Lambda}, z)}, \tag{S2}$$

where $N_{gen}(W, \nu, p_\Lambda, \phi_{\pi^-}, \phi_{e\Lambda}, z)$ and $N_{acc}(W, \nu, p_\Lambda, \phi_{\pi^-}, \phi_{e\Lambda}, z)$ are, respectively, the number of generated and accepted events in each bin $k$. Once these AC coefficients were computed, the data were corrected event-by-event by a weight $\omega_k = 1/AC_k$, which depends on the bin $k$ to which it belongs. It should be noted that if some 6D AC bins have very small correction factors due to their poor statistics, an artificially large weight would be attributed to those bins that would lead to spikes in the weighted distributions. To avoid this problem, the following weight cut was adopted to minimize this effect on the weighted distributions:

$$60 < \omega_k \leq 2400. \tag{S3}$$

Furthermore, the effect of this weight cut was estimated and applied as a global correction factor, $f_\omega$, to the extracted results. This estimation was done by weighting the MC accepted $N_{acc}$ events and comparing their sum, $\sum \omega N_{acc}$, to the generated ones as

$$f_\omega = \frac{\sum \omega N_{acc}}{N_{gen}.} \tag{S4}$$

This $N_{acc}$ weighted sum is typically equal to the generated events without the weight cut, however, it is slightly less once applied, leading to various $f_\omega$ corrections for each $z$-binned multiplicity ratio result as the $p_T$-broadening means are insensitive to this correction.

**SP.3 Systematic Uncertainties Budget**   This section contains the contribution of various systematic effects to the reported total point-to-point systematic uncertainty budget for the $\Lambda$ multiplicity ratios of all nuclei in Table S3 and the corresponding $z$ ($A$) dependence of $p_T$-broadening in Table S4 (S5).

**SP.4 Tabulated Multiplicity Ratio and $p_T$-broadening Results**   This section contains the reported results in the last two figures of this manuscript, Figs. 3 and 4, detailed in Table S6 for all nuclei $z$-binned multiplicity ratios, and Table S7 (Table S8) for all nuclei $z$-binned ($A$-dependent) transverse momentum broadening. In addition, the correlation between $z$ and the Feynman variable $x_F$ is illustrated in Fig. S1 to support the discussion related to the separation between forward and backward fragmentation regions.
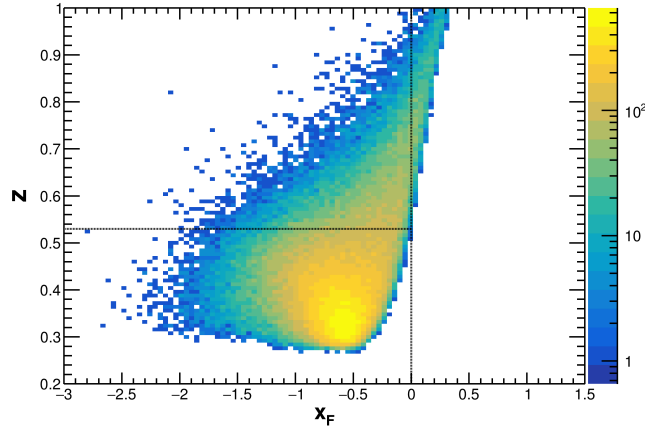


Figure S1. $z$ vs. $x_F$, where the horizontal dashed line around values of $z$ greater than $\sim$0.55 depicts the discussed separation between forward and backward fragmentation regions suggested by the sign change of $x_F$ (vertical dashed line).

Table S3. Multiplicity ratio systematic effects and their contributions for the $z$-bins shown in Table S2.

| Systematic Effect | $z$-bin Point-to-point Systematic Uncertainty (%) | | | | | | | | | | | | | | | | | |
|---|---|---|---|---|---|---|---|---|---|---|---|---|---|---|---|---|---|---|
| | Carbon | | | | | | Iron | | | | | | Lead | | | | | |
| | $z-1$ | $z-2$ | $z-3$ | $z-4$ | $z-5$ | $z-6$ | $z-1$ | $z-2$ | $z-3$ | $z-4$ | $z-5$ | $z-6$ | $z-1$ | $z-2$ | $z-3$ | $z-4$ | $z-5$ | $z-6$ |
| Particle identification cuts | 0.69 | 4.24 | 7.24 | 1.53 | 3.16 | 0.00 | 0.00 | 0.95 | 4.34 | 0.87 | 3.17 | 4.45 | 8.05 | 3.21 | 7.80 | 0.00 | 8.59 | 6.91 |
| Vertex corrections | 0.28 | 0.00 | 0.04 | 0.22 | 0.22 | 0.54 | 1.04 | 1.28 | 0.56 | 0.08 | 0.00 | 0.13 | 1.38 | 1.85 | 0.13 | 0.18 | 0.00 | 1.01 |
| AC 6D map variables & binning | 3.28 | 0.00 | 6.69 | 9.97 | 9.17 | 2.33 | 6.83 | 4.80 | 0.00 | 6.42 | 5.90 | 4.93 | 6.84 | 0.00 | 9.05 | 7.90 | 6.06 | 7.23 |
| AC weight cuts | 0.00 | 0.00 | 10.70 | 0.70 | 0.00 | 0.00 | 0.00 | 0.00 | 9.17 | 1.86 | 0.00 | 0.00 | 5.17 | 0.00 | 8.64 | 12.16 | 0.00 | 0.00 |
| CB uncorrelated-tracks combinations | 1.80 | 0.16 | 0.37 | 0.27 | 0.53 | 0.00 | 1.14 | 0.14 | 0.20 | 0.00 | 0.36 | 0.23 | 1.79 | 2.04 | 0.96 | 0.13 | 0.00 | 0.28 |
| Breit-Weigner shapes | 7.55 | 10.80 | 25.75 | 5.13 | 8.69 | 5.77 | 20.54 | 16.37 | 13.40 | 1.26 | 0.46 | 5.27 | 5.77 | 12.02 | 15.71 | 4.92 | 10.85 | 9.52 |
| $\Lambda$ mass-range | 2.10 | 1.11 | 0.00 | 0.86 | 1.87 | 2.89 | 2.52 | 1.52 | 0.43 | 0.00 | 1.35 | 2.39 | 2.24 | 1.24 | 0.00 | 0.65 | 1.69 | 2.72 |
| LD2 endcaps | 0.06 | 0.00 | 0.06 | 0.09 | 0.11 | 0.13 | 0.03 | 0.00 | 0.06 | 0.08 | 0.10 | 0.12 | 0.07 | 0.00 | 0.05 | 0.07 | 0.09 | 0.13 |
| Radiative correction | 0.00 | 2.08 | 1.26 | 3.18 | 1.53 | 0.94 | 1.30 | 1.14 | 0.29 | 0.00 | 0.95 | 0.21 | 0.13 | 0.00 | 0.81 | 1.12 | 0.58 | 1.90 |
| Total | 8.71 | 11.84 | 29.61 | 11.81 | 13.25 | 6.93 | 21.86 | 17.19 | 16.82 | 6.86 | 6.92 | 8.81 | 13.41 | 12.67 | 21.58 | 15.36 | 15.21 | 14.20 |

Table S4. Transverse momentum broadening systematic effects and their contributions for the $z$-bins shown in Table S2.

| Systematic Effect | $z$-bin Point-to-point Systematic Uncertainty (%) | | | | | | | | | | | | | | | | | |
|---|---|---|---|---|---|---|---|---|---|---|---|---|---|---|---|---|---|---|
| | Carbon | | | | | | Iron | | | | | | Lead | | | | | |
| | $z-1$ | $z-2$ | $z-3$ | $z-4$ | $z-5$ | $z-6$ | $z-1$ | $z-2$ | $z-3$ | $z-4$ | $z-5$ | $z-6$ | $z-1$ | $z-2$ | $z-3$ | $z-4$ | $z-5$ | $z-6$ |
| Particle identification cuts | 7.14 | 0.00 | 3.77 | 1.77 | 0.47 | 6.03 | 1.05 | 8.19 | 4.97 | 0.00 | 0.82 | 0.87 | 5.07 | 2.84 | 6.24 | 0.00 | 3.52 | 3.24 |
| Vertex Corrections | 6.63 | 8.99 | 4.62 | 1.02 | 0.00 | 3.99 | 2.57 | 2.54 | 0.00 | 0.33 | 0.33 | 0.67 | 3.40 | 1.87 | 0.81 | 0.00 | 0.74 | 2.79 |
| AC 6D map variables & binning | 4.77 | 6.95 | 6.02 | 0.00 | 8.91 | 5.49 | 6.36 | 9.72 | 3.05 | 14.85 | 0.00 | 2.20 | 9.84 | 7.83 | 10.52 | 3.83 | 7.73 | 0.00 |
| AC weight cuts | 1.83 | 0.47 | 18.23 | 6.74 | 0.00 | 0.09 | 0.00 | 0.31 | 13.77 | 1.52 | 0.00 | 0.12 | 20.17 | 0.59 | 19.88 | 23.63 | 0.08 | 0.00 |
| CB sideband subtraction | 31.84 | 0.0 | 2.1 | 8.81 | 0.88 | 3.79 | 4.34 | 2.36 | 0.0 | 1.67 | 7.58 | 20.32 | 77.31 | 8.16 | 0.0 | 2.49 | 6.33 | 13.28 |
| Radiative correction | 3.87 | 0.24 | 0.00 | 0.03 | 0.00 | 0.19 | 0.18 | 0.28 | 0.32 | 0.54 | 0.00 | 0.12 | 5.06 | 0.49 | 0.27 | 0.01 | 0.00 | 0.00 |
| Total | 33.88 | 11.38 | 20.21 | 11.28 | 8.96 | 9.84 | 8.19 | 13.18 | 14.96 | 15.04 | 7.63 | 20.46 | 80.89 | 11.84 | 23.35 | 24.07 | 10.62 | 13.95 |

Table S5. $A$-dependent transverse momentum broadening systematic effects and their contributions.

| Systematic effect | Point-to-point Systematic Uncertainty (%) | | |
|---|---|---|---|
| | Carbon | Iron | Lead |
| Particle identification cuts | 4.69 | 1.35 | 0.00 |
| Vertex Corrections | 2.70 | 0.00 | 0.38 |
| AC 6D map variables & binning | 0.57 | 0.00 | 2.21 |
| AC weight cuts | 3.40 | 0.00 | 7.07 |
| CB sideband subtraction | 5.52 | 0.0 | 2.87 |
| Radiative correction | 0.04 | 0.17 | 0.00 |
| Total | 8.46 | 1.36 | 7.96 |

Table S6. Measured Λ z-binned multiplicity ratios for all nuclei along with their total statistical and systematic (point-to-point and normalization uncertainties depicted in Fig. 3 added in quadrature) uncertainties.

| z-bin | $R_\Lambda^A \pm$ Statistical $\pm$ Systematical Uncertainties | | |
|---|---|---|---|
| | Carbon | Iron | Lead |
| 0.28 - 0.38 | $3.4256 \pm 0.5319 \pm 0.3004$ | $5.7536 \pm 0.5681 \pm 1.2661$ | $7.2363 \pm 0.9997 \pm 0.9893$ |
| 0.38 - 0.44 | $1.3447 \pm 0.1603 \pm 0.1628$ | $1.9382 \pm 0.1769 \pm 0.3629$ | $2.6378 \pm 0.3405 \pm 0.3863$ |
| 0.44 - 0.51 | $1.1084 \pm 0.1205 \pm 0.3299$ | $2.0100 \pm 0.1735 \pm 0.3674$ | $2.1293 \pm 0.2316 \pm 0.4987$ |
| 0.51 - 0.60 | $1.1498 \pm 0.0883 \pm 0.1400$ | $1.2126 \pm 0.0823 \pm 0.1663$ | $1.1857 \pm 0.1057 \pm 0.2659$ |
| 0.60 - 0.75 | $1.1174 \pm 0.0756 \pm 0.1519$ | $0.9660 \pm 0.0617 \pm 0.1588$ | $0.8910 \pm 0.0759 \pm 0.2364$ |
| 0.75 - 1.00 | $0.9506 \pm 0.1011 \pm 0.0741$ | $0.6450 \pm 0.0529 \pm 0.1549$ | $0.5622 \pm 0.0621 \pm 0.2096$ |

Table S7. Measured Λ z-binned $p_T$-broadening results for all nuclei with their total statistical and systematic (point-to-point and normalization uncertainties depicted in Fig. 4 left added in quadrature) uncertainties.

| z-bin | $\Delta p_T^2$ (GeV$^2$) $\pm$ Statistical $\pm$ Systematical Uncertainties | | |
|---|---|---|---|
| | Carbon | Iron | Lead |
| 0.28 - 0.38 | $0.0003 \pm 0.0143 \pm 0.0015$ | $0.0112 \pm 0.0127 \pm 0.0015$ | $-0.0072 \pm 0.0151 \pm 0.0060$ |
| 0.38 - 0.44 | $0.0259 \pm 0.0160 \pm 0.0033$ | $0.0422 \pm 0.0140 \pm 0.0057$ | $0.0592 \pm 0.0171 \pm 0.0071$ |
| 0.44 - 0.51 | $0.0648 \pm 0.0174 \pm 0.0132$ | $0.0894 \pm 0.0147 \pm 0.0134$ | $0.0613 \pm 0.0174 \pm 0.0144$ |
| 0.51 - 0.60 | $0.1317 \pm 0.0165 \pm 0.0149$ | $0.2120 \pm 0.0168 \pm 0.0319$ | $0.2007 \pm 0.0211 \pm 0.0483$ |
| 0.60 - 0.75 | $0.1879 \pm 0.0225 \pm 0.0169$ | $0.2591 \pm 0.0218 \pm 0.0198$ | $0.3140 \pm 0.0295 \pm 0.0334$ |
| 0.75 - 1.00 | $0.1145 \pm 0.0157 \pm 0.0114$ | $0.1381 \pm 0.0149 \pm 0.0283$ | $0.1788 \pm 0.0209 \pm 0.0250$ |

Table S8. Measured Λ A-dependent $p_T$-broadening results for all nuclei along with their total statistical and systematic (point-to-point and normalization uncertainties depicted in Fig. 4 right added in quadrature) uncertainties.

| A | $\Delta p_T^2$ (GeV$^2$) $\pm$ Statistical $\pm$ Systematical Uncertainties |
|---|---|
| Carbon | $0.0952 \pm 0.0272 \pm 0.0082$ |
| Iron | $0.1404 \pm 0.0376 \pm 0.0024$ |
| Lead | $0.1823 \pm 0.0451 \pm 0.0146$ |